Electronic Supplementary Material (ESI) for Chemical Communications.

This journal is © The Royal Society of Chemistry 2020

Supporting Information

Amorphous-MoO_{3-x}/MoS_2 heterostructure: *in-situ* oxidizing amorphization of S-vacancy MoS_2 for enhanced alkaline hydrogen evolution

Wenzhuo Wu,[#a] Chunyao Niu,[#b] Qingyong Tian,[a] Wei Liu,[a] Guowei Niu,[a] Xiaoli Zheng,[a] Chong Li,[b] Yu Jia,*[b,c] Cong Wei,[a] Qun Xu*[a]

[a]*College of Materials Science and Engineering, Zhengzhou University, Zhengzhou 450052 (China).*

[b]*International Laboratory for Quantum Functional Materials of Henan, School of Physics and Microelectronics, Zhengzhou University, Zhengzhou 450001 (China).*

[c]*Key Laboratory for Special Functional Materials of Ministry of Education & School of Materials Science and Engineering, Henan University, Kaifeng 475004 (China).*

Experimental Procedures

Chemicals.

The Molybdenum disulfide (MoS_2) was purchased from Sigma-Aldrich. Sodium borohydride ($NaBH_4$), hydrochloric acid (HCl)，sulfuric acid (H_2SO_4), potassium hydroxide (KOH, 99%), platinum carbon black (Pt/C, 20%), ethanol and nickel foam (Ni-f) used were purchased from Sinopharm Chemical Reagent Co., Ltd. (China) and used without further treatment. Nitrogen with a purity of 99.99% was provided by the Zhengzhou Shuang yang Gas Co., Ltd. (China) and used as received. Deionized (DI) water with a resistivity of 18.2 MΩ·cm was prepared via a Milli-Q Water Purification System.

Ultrasonic exfoliation of MoS_2nanosheets

200 mg of MoS_2 powder was firstly added to a 500 mL flask. After adding 40 mL of ethanol/water (v/v1/1) mixtures, the sealed flask was sonicated in the the sonication bath for 5 h. Then the dispersion was centrifuged at 5000 rpm for 30 mins to remove aggregates. The ultrasonication exfoliated MoS_2 nanosheets in supernatant was. collected and diluted for TEM characterization.

Synthesis of Sv-MoS_2nanosheets

The production of Sv-MoS_2 nanosheets was carried out through the previously reported solid-phase reduction process using $NaBH_4$as reductant. Initialy, 1 g of $NaBH_4$ and bulk MoS_2 was mixed through sufficient grinding (15 min). Then the mixture was put into furnace, blowed with high-pruity nitrogen gas at 60 °C for 30 min, and heated to 380 °C with a heating rate of 10 °C per min for 2 h. After cooling down to room temperature, the mixture was added slowly into a flask with 1M HCl solution and vigorously stirred for 30 min. After that, the mixture was washed by water for several times till the supernatant liquid turned cloudy after high-speed (10000 rpm) centrifugation. Then the dispersion was centrifuged at 5000 rpm for 30 mins to remove aggregates. Finally, the product in supernatant was washed by water and ethanol and was separated after a high-speed centrifugation and drying in a vacuum oven.

Synthesis of amorphous MoO_{3-x}/MoS_2 heterostructure

Ten milligrams of dried Sv-MoS_2 nanosheets sediment were dissolved in 30 ml of ethanol /water (v/v 1/1) mixtures and sonicated in the sonication bath for 5 h. Then, the black solution was transferred into an autoclave and loaded into a furnace, which has been heated to 120 °C. The temperature of the oven was maintained at 120 °C overnight. Next, the reaction was terminated by rapidly cooling the solution to room temperature by removing the autoclave from the oven. The prepared products were seperated from the light blue solution by centrifugation and washed with deionized water and ethyl alcohol several times. The amorphous-MoO_{3-x}/MoS_2 were dried at 40 °C overnight to obtain the heterostructure through a vacuum oven, and the two-dimensional heterostructures were obtained with different hydrothermal temperatures.

Characterization

The morphology of the samples was measured by using a transmission electron microscopy (TEM) JEM-2100 (JEOL, Japan). The elemental mapping images were taken using FEI Tecnai G2 F20 S-TWIN operating at 200 kV. X-Ray diffraction (XRD) patterns of the samples were collected on a Rigaku D/Max 2550 X-ray diffractometer with Cu Kα radiation (λ= 1.5418 Å).Raman analysis was carried out on aninVia Raman spectrometer (Renishaw, UK) with 532 nm wavelength incident laser light. The X-ray photoelectron spectroscopy (XPS) measurements were performed on an XPS, ESCA Lab250 X-ray photoelectron spectrometer (Thermo Fisher Scientific, USA) with Al Kα source. All XPS spectra were corrected using C 1s line at 284.6 eV, and curve fitting and background subtraction were accomplished.

Electrochemical Characterizations

The electrochemical HER experiments were performed in a standard three-electrode glass cell connected to a CHI 660D workstation using as-prepared catalysts loaded glassy carbon electrode (GCE) or nickel foam (Ni-f) as the working electrode, Platinum wire as counter electrode and Ag/AgCl (acidic) or Hg/HgO (alkaline) electrode as the reference electrodes. All potentials used in this work have been converted to the RHE scale (Potential = $E_{Ag/AgCl}$+ 0.059 × pH + 0.197 or $E_{Hg/HgO}$+ 0.059 × pH + 0.098). The catalysts (4.0 mg) were ultrasonically dispersed in 2 mL ethanol/water mixture (1/1, v/v) containing 10 μLNafion solution as the binder, then homogeneous catalyst ink was drop-coated onto the GC electrode ($A_{geometric}$ = 0.19625 cm^2) or Ni foam electrode ($A_{geometric}$ = 0.785 cm^2). The catalyst loading was 0.2 mg/cm^2. Polarization curves were measured at a scan rate of 5 mV s^{-1}. The electrochemical impedance spectrum (EIS) was carried out in the frequency range from 1 M to 0.1 Hz. Cyclic voltammetry curves in the region of 0.1-0.2 V *vs.* RHE. were measured under different scan rates. These data were used to caculate the electrochemical double-layer capacitance (C_{dl}). The real surface area for HER is calculated from the electrochemical active surface areaECSA, which can be calculated by the C_{dl} value. The specific capacitance for a flat surface is generally reported to be in the range of 20-60 μF cm^2_{geo}. In the following calculations, we assume an average value of specific capacitance vaule is 40 μF cm^2_{geo}.

Calculation methods

All the calculations are based on Density Functional Theory (DFT) as implemented in the Vienna Ab-initio Simulation Package (VASP) code,[1,2] utilizing the projector augmented wave method (PAW),[3] The exchange-correlation energy of generalized gradient approximation put forward by Perdew, Burke, and Ernzerhof (GGA-PBE) [4] is adopted, and the vdW interaction is treated using the DFT-D3 method proposed by Grimme.[5] A vacuum of 15 Å perpendiculars to the sheets was applied to avoid the interaction between layers. A kinetic energy cutoff of 450 eV is used for the plane wave basis set. For Brillouin zone integration, the 2×2×1 k-point mesh and the Gama point were used for the Sv-MoS_2 and A-MoO_{3-x}, respectively. Convergence criteria employed for both the electronic self-consistent relaxation and ionic relaxation are set to be 10^{-4} and 0.03 eV/Å for energy and force, respectively. To evaluate the energy barrier, the transitional state (TS) was located using the nudged elastic band (NEB) method.[6] The energy barriers (E_b) were calculated according to $E_b = E_{TS} – E_{IS}$, where E_{IS} and E_{TS}were the energies of the corresponding initial state (IS)and transition state (TS), respectively.

DFT Models:

The Sv-MoS_2 system is constructed with a 2×2 supercell containing one S vacancy (S vacancy density 3.125%, Scheme 1). For the simulation of amorphous MoO_{3-x} (A-MoO_{3-x}) monolayers, we used a 6×6×1 supercell with about 10% O vacancies, according to our experiments (Scheme 2). Here it is worthy to note that the size of the supercell (~3 nm) is large enough to simulate the following the molecular dynamic (MD). The MD simulations which lasted for 6 ps are performed in the canonical (NVT) ensemble at temperature of 1000K. The structure is fully relaxed in 0 K after the MD simulations to get the final A-MoO_{3-x} monolayers.

The construction of amorphous MoO_{3-x}/MoS_2 heterostructure need much more atoms which is much computation time consuming for the DFT NEB calculations. However, we should note that the adsorption energies as well as the energy barriers are not sensitive to the layered Van der Waals heterojunction. Also, the interfacial electrical which is very important in the HER performance can be well described by the alignment of the fermi levels of the two components. In all, the models in the computations are reasonable and the results are reliable.

The Gibbs free energy change (ΔG) for each step of the HER was calculated as follows:

$$\Delta G = \Delta E + \Delta ZPE - T\Delta S \ (T = 300\ K) \quad (1)$$

where ΔE, ΔZPE and ΔS are the changes in the adsorption energy, zero-point energy and entropy, respectively.

The zero-point energy and entropy correction were obtained from the NIST-JANAF thermodynamics table[7] for gas molecules, and by calculating the vibrational frequencies for the intermediate adsorbates, respectively.

The adsorption energy (Ea) of X (X= H, OH, and H_2O) is computed using the following equation:

Ea = E(total) - E(sub) - E(X);

where E(total), E(sub) and E(X) are the total energies of a supercell with and without X adsorbed,

respectively, and E(X) is the total energy of the X atom.

Based on the Tafel-Heyrovsky-Volmer mechanism, there are three elementary reaction steps for the HER on the catalyst's surfaces in alkaline solution.

Volmer step: $H_2O + e^- \longrightarrow H_{ad} + OH^-$

Heyrovsky step: $H_2O + H_{ad} + e^- \longrightarrow H_2 + OH^-$

Tafel step: $2H_{ad} \longrightarrow H_2$

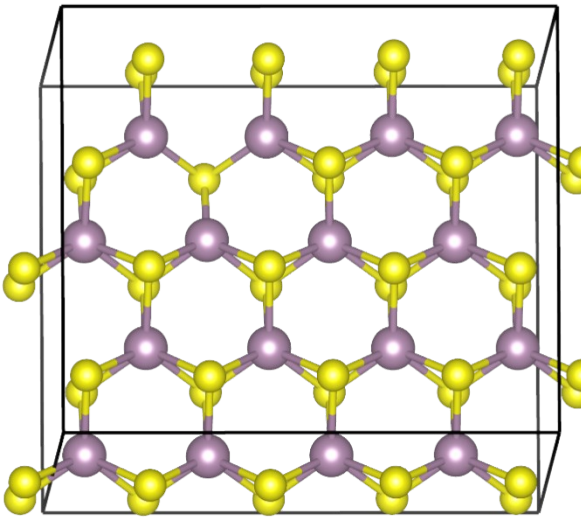

Scheme S1. Schematic crystal structures of Sv-MoS_2 used in DFT simulation.

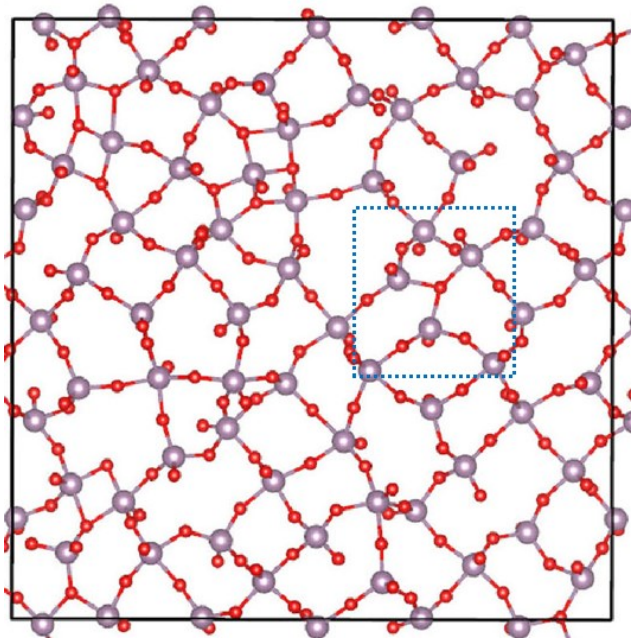

Scheme S2. Schematic crystal structures of amorphous MoO_{3-x} used in DFT simulation. The selected adsorption area is denoted by blue dot box.

Supporting Results

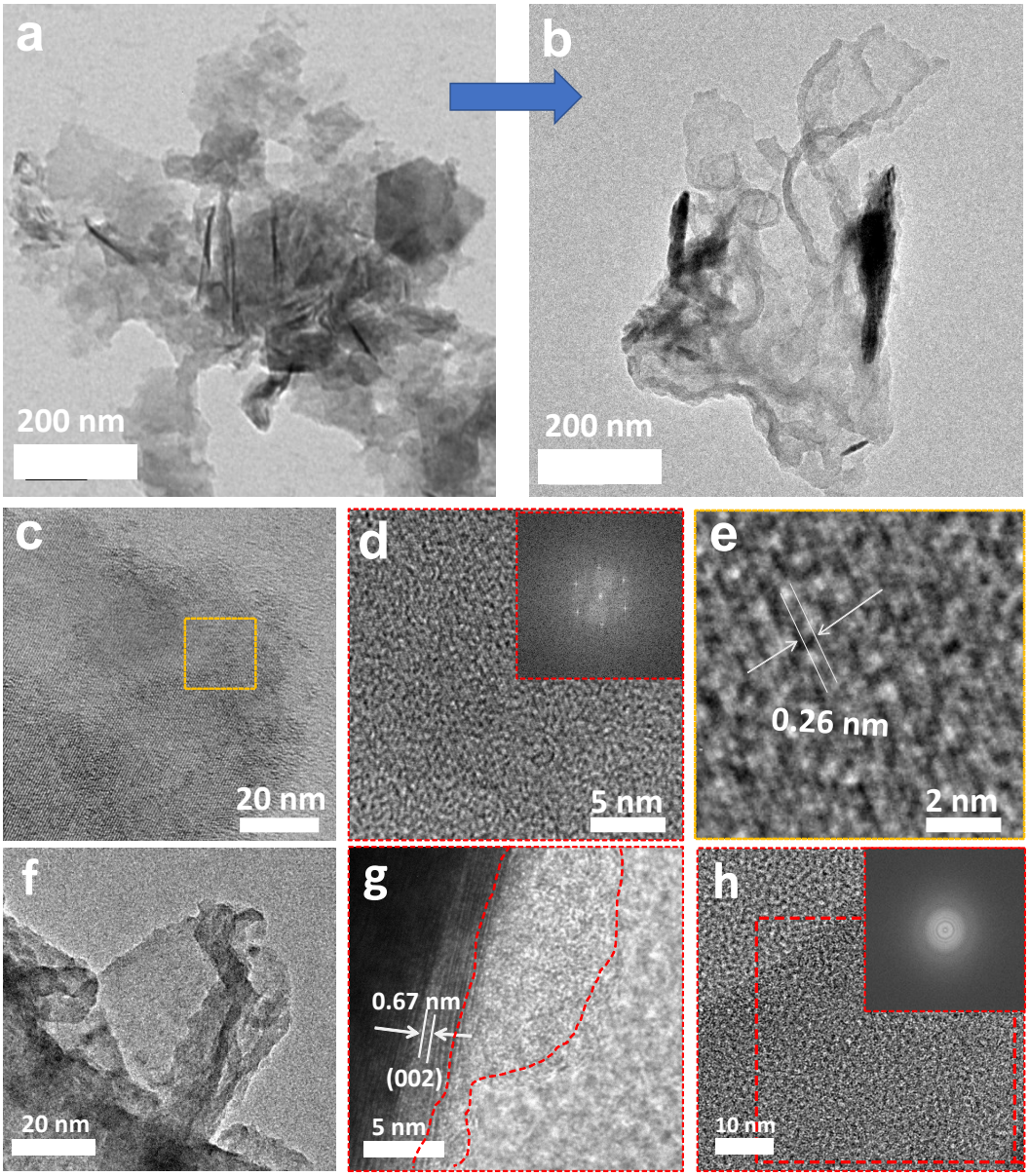

Figure S1. TEM images and FFTof as-prepared Sv-MoS_2 particles (a, c-e) and A-MoO_{3-x}@MoS_2 heterostructure (b, f-h).

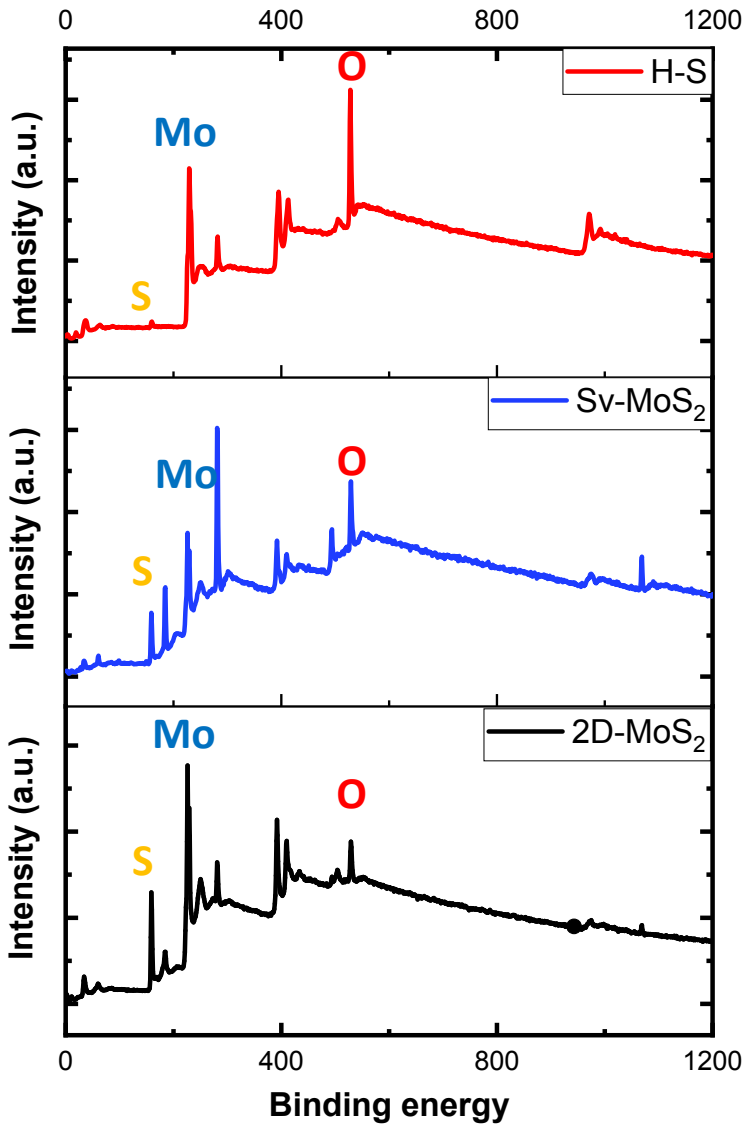

Figure S2. XPS survey scan of 2D-MoS_2, Sv-MoS_2, and amorphous-MoO_{3-x}/MoS_2 heterostructure (H-S), respectively.

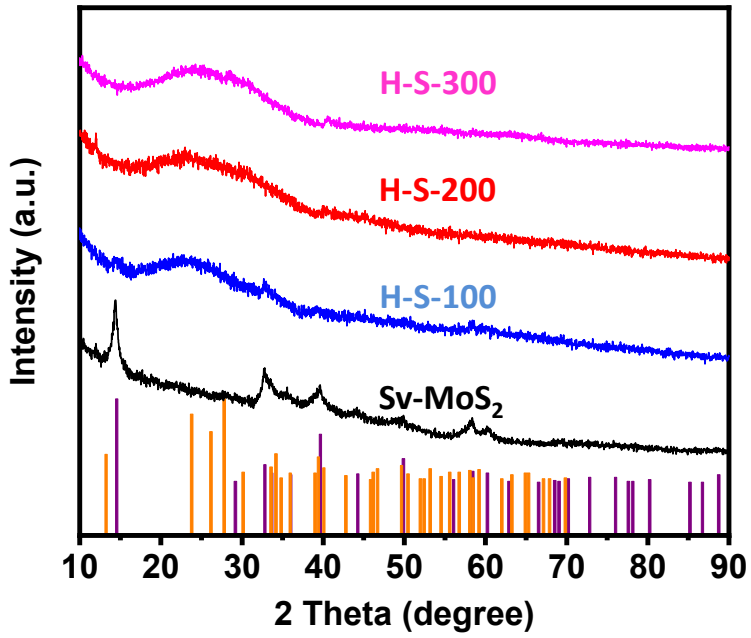

Figure S3. XRD spectra of as-prepared amorphous MoO_{3-x}/MoS_2 heterostructure (H-S-x).x-Sv-MoS_2 (x = 100, 200 and 300, the mass weight ratio of reductant to MoS_2 is 100,200 and 300% in SPR process) are used as the initial template. As shown in the spectra, the typical (002) peak of MoS_2 is absent in the resultant MoO_{3-x}/MoS_2-200 (H-S-200) and H-S-300, indicating the surface of the materials have been fully oxidized.

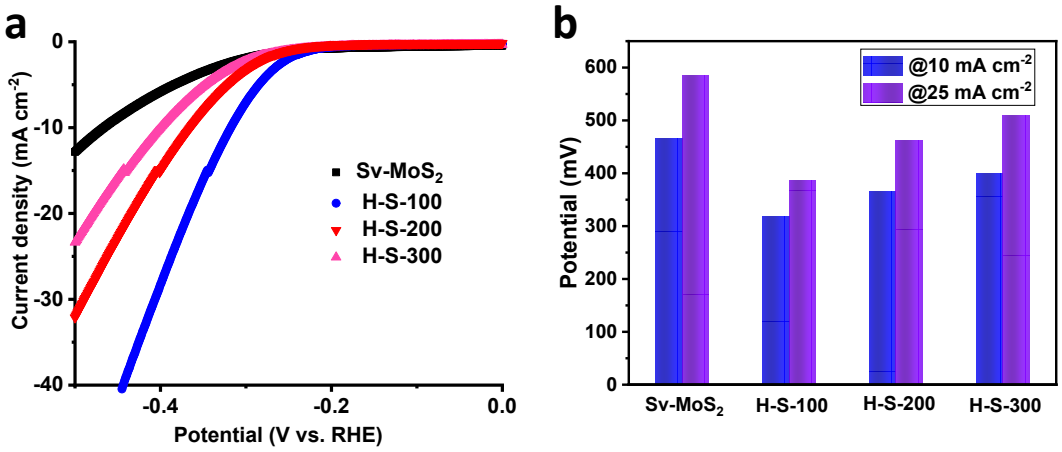

Figure S4. (a) Polarization curves of as-prepared amorphous MoO_{3-x}/MoS_2 heterostructure (H-S-x). (b) Potentials at current densities of 10 and 25 $mAcm^{-2}$. The measurements are conducted in 1 M KOH.

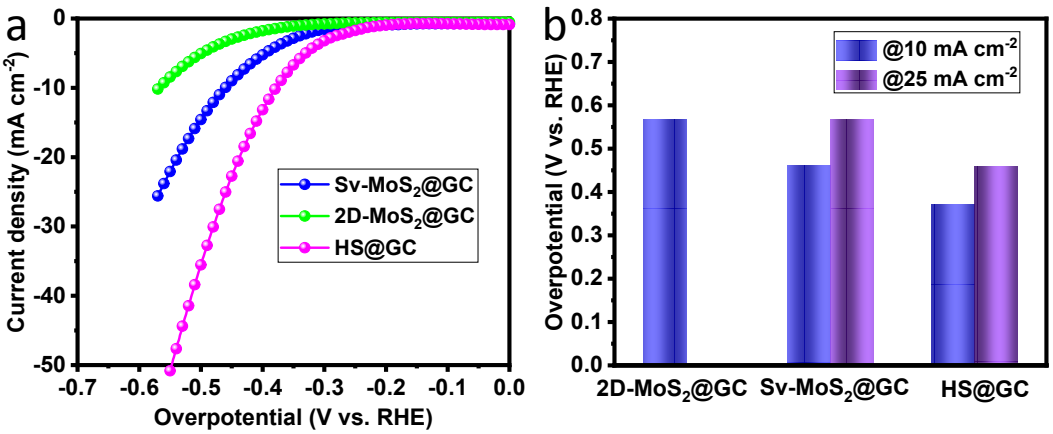

Figure S5. (a) Polarization curves of 2D-MoS_2, Sv-MoS_2, and amorphous-MoO_{3-x}/MoS_2 heterostructure (HS). (b) Potentials at current densities of 10 and 25 $mAcm^{-2}$. The measurements are conducted in 1 M KOH. In this comparation experiment, the HER performance of A-MoO_{3-x}/MoS_2 (HS) catalyst is obviously superior to the completely oxidized A-MoO_{3-x} and Sv-MoS_2 in alkaline, suggesting that the synergy of A-MoO_{3-x} and Sv-MoS_2 in heterojunction can further enhance the HER performance.

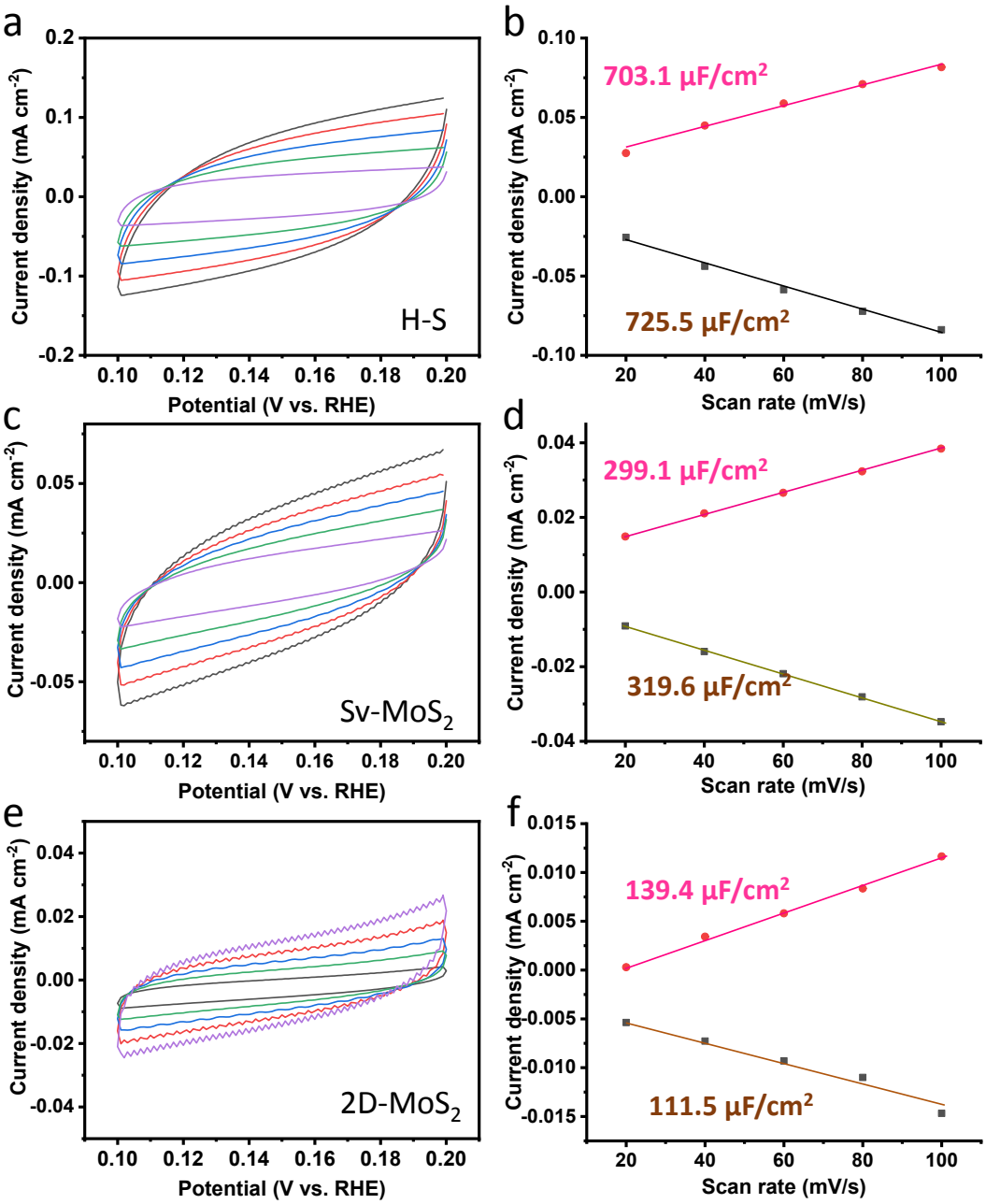

Figure S6. Electrochemical capacitance measurements to determine the ECSA.

The The detailed analysis of the intrinsic HER activity (Fig. 3d), charge-tranfer ability (Fig. 3e), stability (Fig. 3f) and HER performance (Fig. 3g):

To compare the intrinsic HER activity, the as-calculated ECSA is applied to identify the catalysts' intrinsic activity.[8] As shown in Figure 3d, A-MoO_{3-x}/MoS_2 delivers the j_{ECSA} value of 1.32A cm^{-2} at η = 200 mV, which is markedly higher than those of 2D-MoS_2 (0.41 A cm^{-2}) and Sv-MoS_2 (0.39 A cm^{-2}). These results indicate that A-MoO_{3-x}/MoS_2 has higher intrinsic HER catalytic capacity than 2D-MoS_2 and Sv-MoS_2 in alkaline electrolyte. The electrochemical impedance spectroscopy (Figure3e) shows that A-MoO_{3-x}/MoS_2 on Ni foam yields small charge-transfer resistance (Rct) (2 ohms) in 1.0 M KOH, which is much lower than that of 2D-MoS_2@Ni-f and Sv-MoS_2@Ni-f (5 ohms), indicating that the introduced A-MoO_{3-x} facilitate the electron transport at the electrode/electrolyte interface. Likewise, this phonomenon has also been evidenced in acidic solution (Figure S8). The electrochemical and structural stability of A-MoO_{3-x}/MoS_2 was demonstrated by the results in Figure 3f and Figure S11-13. Most importantly, the alkaline condition HER activity of the as-designed A-MoO_{3-x}/MoS_2 outperform many reported non-precious metal-based electrocatalysts (Figure 3g, TableS2).

Figure S7. Photo of Sv-MoS_2 and amorphous MoO_{3-x}/MoS_2 heterostructure (HS) loaded on Ni foam.

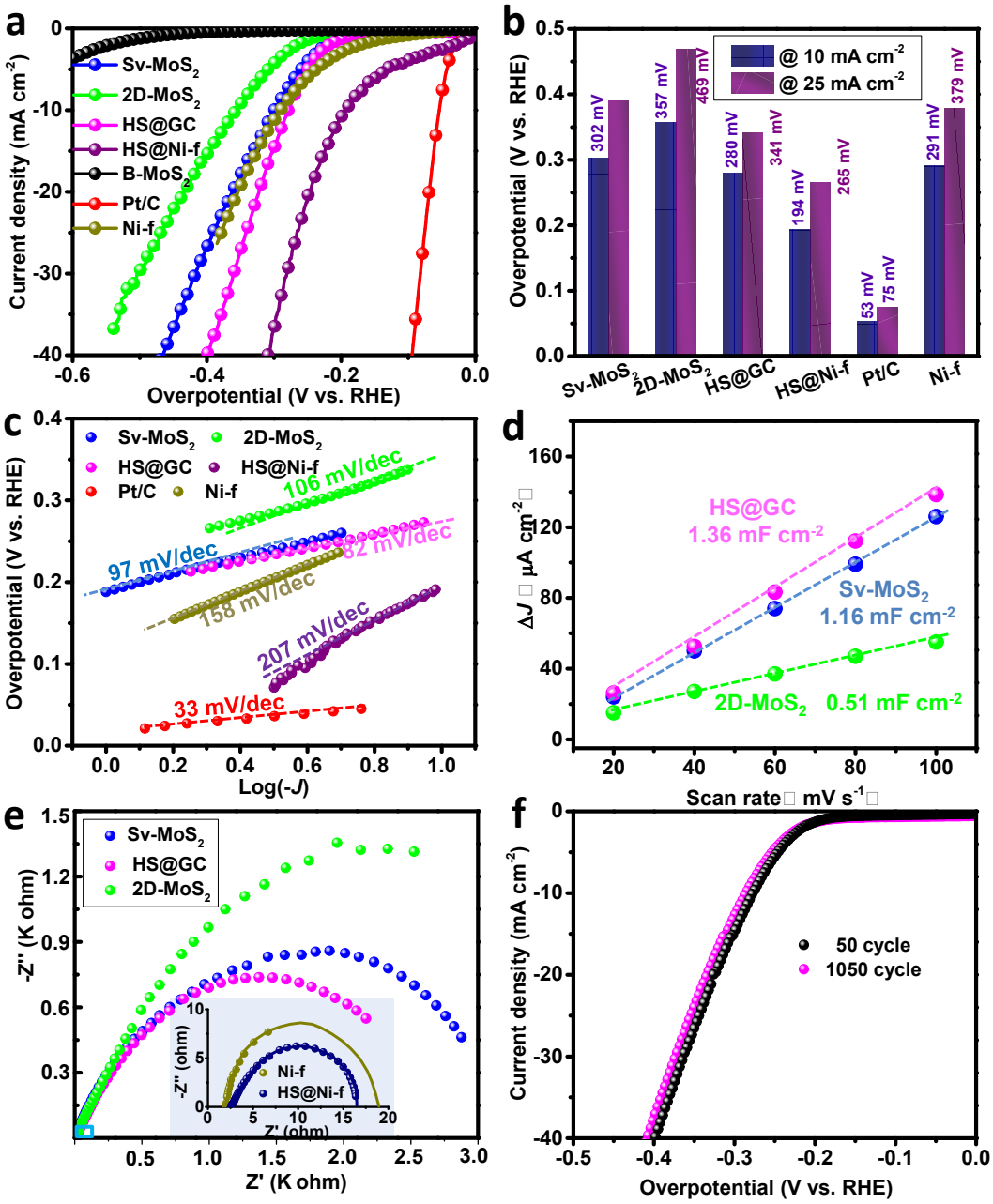

Figure S8. HER activity of the synthesized samples. (a) Polarization curves of bulk MoS_2, P-MoS_2 nanosheets, Sv-MoS_2 nanosheets, MoO_{3-x}@MoS_2 heterostructure and Pt/C. (b) Potentials at current densities of 10 and 25 mAcm^{-2}. (c) Corresponding Tafel plots obtained from the polarization curves. (d)Electrochemical capacitance measurements. (e) EIS of MoO_3@MoS_2 heterostructure, P-MoS_2nanosheets, and Sv-MoS_2 nanosheets. (f) Electrochemical stability test of MoO_3@MoS_2 heterostructure.

Adsorption configurations:

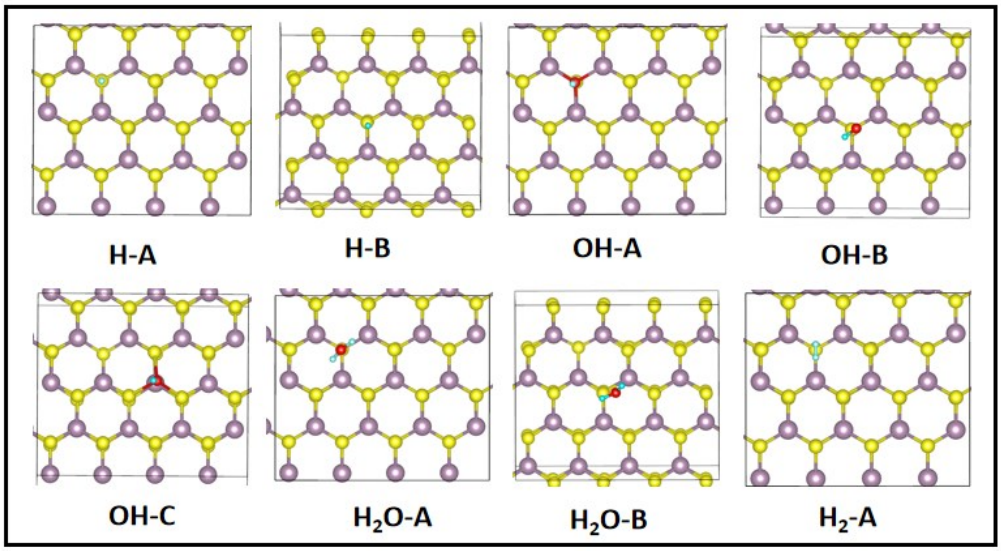

Figure S9. The adsorption configurations of H, OH and H_2O on the Sv-MoS_2.

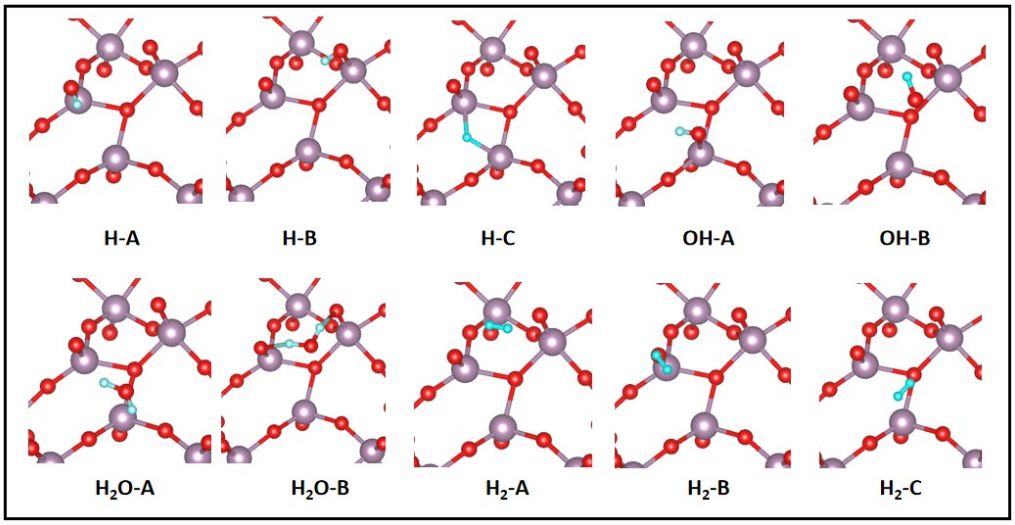

Figure S10. The adsorption configurations of H, OH and H_2O on the A-MoO_{3-x}.

Table S1. The Adsorption energy (E_a) of H, OH and H_2O on the Sv-MoS_2 and A-MoO_{3-x} as shown in Figure S9 and S10

Sv-MoS_2		A-MoO_{3-x}	
Adsorption configurations	E_a (eV)	Adsorption configurations	E_a (eV)
H-A	-2.485	H-A	-2.006
H-B	-1.034	H-B	-2.004
OH-A	-3.850	H-C	-1.640
OH-B	-1.230	OH-A	-1.970
OH-C	-0.221	OH-B	-0.268
H_2O-A	-0.156	H_2O-A	-0.457
H_2O-B	-0.09	H_2O-B	-0.241
H_2	-0.096	H_2-A	-0.02
		H_2-B	-0.08

For the Sv-MoS_{2-x}, we found that H, OH and H_2O are all prefer to adsorb at the S vacancy site and the adsorption energy of OH is much larger than that of H. And the OH occupies the active sites and reduces the HER in Sv-MoS_2. Moreover, the adsorption energy of H_2O is also very weak, suppressing the initial water adsorption in the Volmer step. The overall structure of A-MoO_{3-x} is complex, however, the local structure at the adsorption sites are similar. Further we checked that the adsorption energies of H on different O sites are close (see table S1 H-A and H-B). Compared to that in Sv-MoS_2, the adsorption energy of OH is reduced while that of H_2O is enhanced in the A-MoO_{3-x} systems, suggesting that the initial water adsorption step and the concomitant adsorption of the formed OH can be effectively promoted. What is more, the preferable adsorption sites for OH and H are different with OH at Mo sites and H at O sites, respectively. The separation of OH and H avoid the concomitant of active sites by OH, boosting the HER kinetics in A-MoO_{3-x}.

The detailed analysis of interfacial electrical which can promote the overall water splitting activity (Fig. 4c,d):

It has shown that the interfacial electrical can promote the overall water splitting activity effectively. To analyze the charge transfer in the interface of A-MoO_{3-x}/MoS_2 heterojunction, we plot in Figure 4c the total electron density of states (TDOS) for Sv-MoS_2 and A-MoO_{3-x}. Their Fermi level are -4.02 and -4.97 eV for Sv-MoS_2 and A-MoO_{3-x}, respectively (energy vs. the vacuum level). At the A-MoO_{3-x}/MoS_2 interface, electron transfer from MoS_2 to A-MoO_{3-x} occurs to align the fermi levels of the two components, resulting in a contact electric potential (CEP) of ~0.95 V across the interface (Figure 4d). This CEP acts as an additional electric potential versus the reversible hydrogen electrode, which can facilitate electrochemical reactions. In all, the low energy barrier of water dissociation and H_2 formation, more effective active sites, as well as the interface electric field account the high HER performance in the in A-MoO_{3-x}/MoS_2 heterojunction.

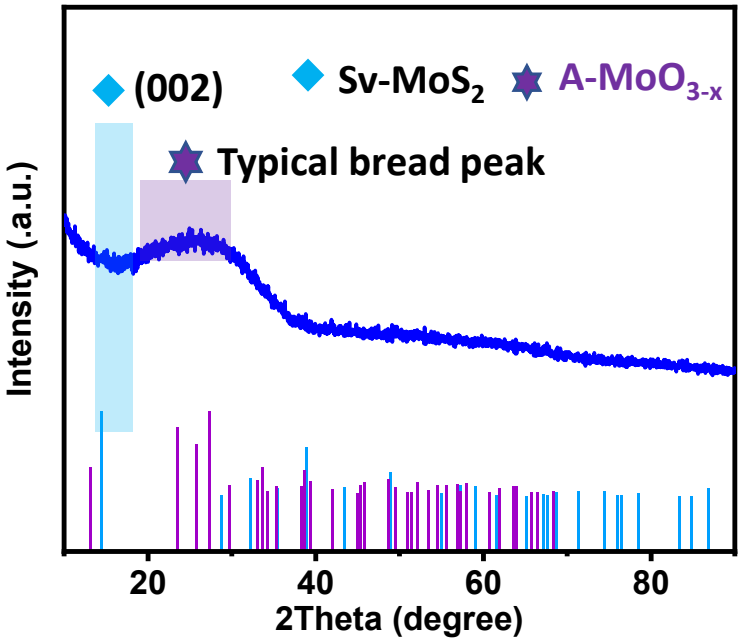

Figure S11. XRD pattern of A-MoO_{3-x}/MoS_2 heterostructure after electrocatalytic HER stability test.

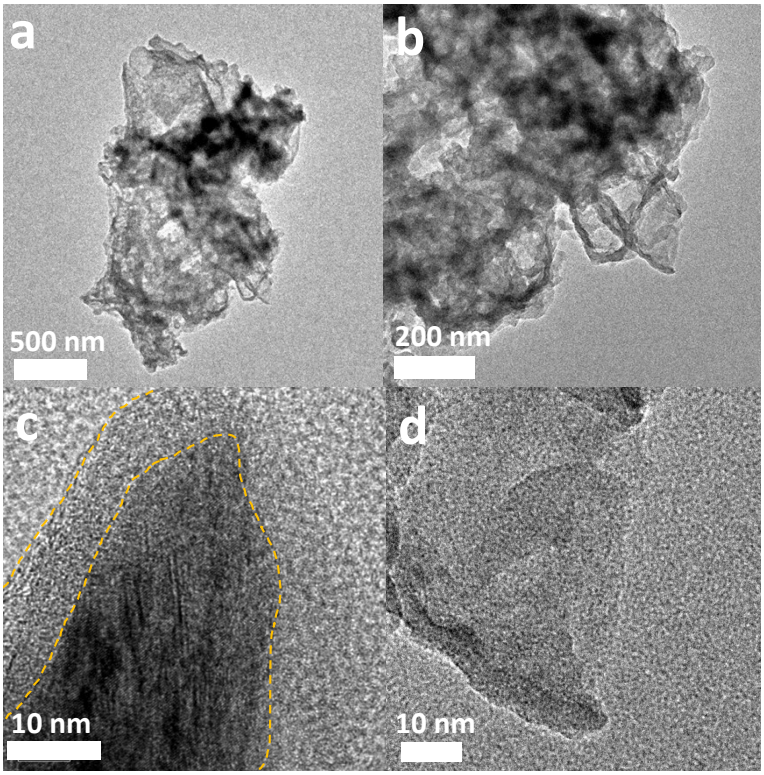

Figure S12. (a, b). TEM images of A-MoO_{3-x}/MoS_2 heterostructure after electrocatalytic HER stability test. (c, d) enlarged TEM images of the selected region of (a, b).

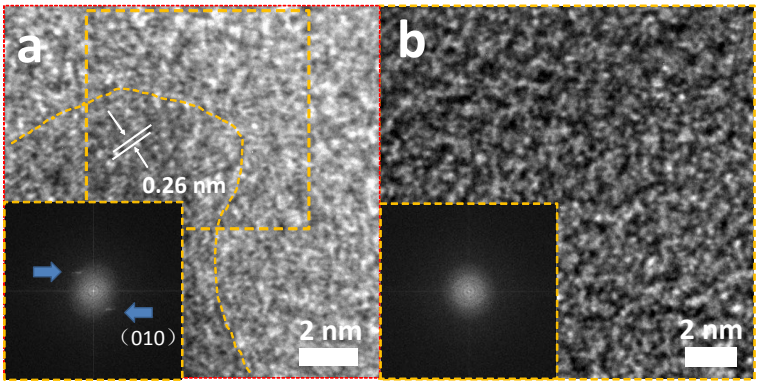

Figure S13. High resolution TEM images of A-MoO_{3-x}/MoS_2 heterostructure after electrocatalytic HER stability test. (a) HRTEM image of a selected heterostructure region from Figure S12c, inset is the FFT pattern of the boxed region; (b) HRTEM image of a selected region from Figure R 12d, inset is the FFT pattern.

Table S2. Comparison of the electrocatalytic HER performance of non-precious metal-based electrocatalysts in 1 M KOH.

Catalyst	η (mV vs. RHE) @ J= -10 mA cm^{-2}	Ref.
MoS_{2-x} @MoO_{3-x}	**146**	**This work**
MoC_x nano-octahedrons	151	*Nat Commun.* **2015**, *6*, 6512.
Mo_2N@Mo_2C/GO	154	*Adv. Mater.* **2018**, *30,* 1704156.
MoS_2/Co_3S_4	152	*Adv. Funct. Mater.* ***2020****, 30, 1908520.*
Ni_2P/MoO_2@MoS_2/Ti-f	159	*Nanoscale* **2017**, *9,* 17349.
Amorphous MoS_x film /	160	*Acc. Chem. Res.* ***2014****, 47, 2671.*
CoN_x/C	170	*Nat. Commun.* **2015**, *6*, 7992.
Co/β-Mo_2C@N-CNTs	170	*Angew. Chem. Int. Ed., 10.1002/anie.201814262.*
CoMnCH/Nif	180	*J. Am. Chem. Soc.* ***2017****,139, 8320.*
CP/CTs/Co-S	190	*ACS Nano* ***2016****, 10, 2342.*
NiCoP/rGO	209	*Adv. Funct. Mater.* ***2016****, 26, 6785.*
$NiCo_2S_4$ NW/Ni-f	210	*Adv. Funct. Mater.* ***2016****, 26, 4661.*
NiFe-LDH/Ni-foam	210	*Science,* ***2014****, 345, 1593.*
Co_3O_4/MoS_2	205	*Appl. Catal., B,* ***2019****, 248, 202–210.*
H-$MnMoO_4$/Ni-f	~220	*J. Mater. Chem. A.* ***2016****, 6, 1600528.*
$Cu_{0.3}Co_{2.7}P$/NC	220	*Adv. Energy Mater.* ***2017****, 7, 1601555.*
Ni_3S_2/Ni-f	223	*J. Am. Chem. Soc.* ***2015****, 137, 14023.*
NiS-$Ni(OH)_2$@MoS_{2-x}	226	*Adv. Funct. Mater.,* ***2016****, 26, 7386.*
$Co_{0.85}Se$/NG	227	*J. Power Sources* ***2018****, 400, 232.*
Ni_9S_8/Ni	230	*Adv. Funct. Mater.* ***2016****, 26, 3314.*
CoOx@CN/GC	232	*J. Am. Chem. Soc.* ***2015****, 137, 2688.*
Co0.85Se/NiFe-LDH	260	*Energy Environ. Sci.* ***2016****, 9, 478.*
1D MoO_x/MoS_2	259	*Angew. Chem. Int. Ed.* **2016**, 55, 12252-12256.

NiMo NWs/Ni-f	270	*Nano Energy.* ***2016****, 27, 247.*
$MoSe_2/SnS_2$	285	*Nano Energy,* ***2019****, 64, 103918.*
NiFe LDH-NS/DG-10	300	*Adv. Mater.* ***2017****, 29, 1700017.*
$Ni(OH)_2@MoS_2@CC$	119	Nano Energy, **2017**, 37,74-80.

References

[1] a) G. Kresse, J. Hafner, *Phys. Rev.* B **1993**, 47, 558-561; b) G. Kresse, J. Furthmüller, *Comput. Mater. Sci.* **1996**, *6*, 15-50.

[2] J. P. Perdew, K. Burke and M. Ernzerhof, *Phys. Rev. Lett.* **1996**, *77*, 3865-3868.

[3] S. Grimme, J. Antony, S. Ehrlich and S. Krieg, *J. Chem. Phys.* **2010**, *132*, 154104.

[4] P. E. Blchl, *Phys. Rev. B* **1994**, *50*, 17953–17979.

[5] J. Lee, S. Kang, K. Yim, K.Y. Kim, H.W. Jang, Y. Kang, S. Han, *J. Phys. Chem. Lett.***2018**, *9*, 2049-2055.

[6] G. Henkelman, H. Jónsson, *J. Chem. Phys.* **2000**, *113*, 9978.

[7] Chase, M. W. NIST-JANAF Thermochemical Tables, American Chemical Society, New York, **1998**.

[8] Y. Zhu, H. A. Tahini, Z. Hu, J. Dai, Y. Chen, H. Sun, W. Zhou, M. Liu, S. C. Smith, H. Wang and Z. Shao, *Nat. Commun.* **2019**, *10*, 149.